PAPER • OPEN ACCESS

Shock-free ion transmission in a skimmer-based MEMS mass spectrometer vacuum interface

View the article online for updates and enhancements.

Shock-free ion transmission in a skimmer-based MEMS mass spectrometer vacuum interface

S Wright[1] and R R A Syms[2]

[1] Microsaic Systems, GMS House, Boundary Road, Woking, Surrey GU21 5BX, United Kingdom
[2] EEE Department, Imperial College London, Exhibition Road, London SW7 2AZ, United Kingdom

E-mail: r.syms@imperial.ac.uk

CrossMark

Abstract

Shock-free ion transmission from atmospheric pressure to a microelectromechanical system (MEMS)-based mass spectrometer has been achieved using micro-engineered nickel skimmers. The signal level has increased 70-fold compared with a previous configuration in which the skimmer did not sample the supersonic flow. The skimmers are formed by electroplating internal surfaces of anisotropically etched, pyramidal holes in (100) silicon. Etching from the reverse of the wafer exposes free-standing, open-ended skimmers supported by remaining silicon. High-resolution schlieren imaging has been used to visualise gas flow within the interface. Signal enhancement and increased gas throughput are observed when the skimmer attaches to the supersonic gas expansion via oblique shocks. The silicon back wall interacts with the flow field, causing the free jet Mach disc to evolve into a bowl-shaped surface shock whose position asymptotically approaches a stand-off separation as the interface pressure decreases. Ideally, the skimmer entrance should be located approximately midway between the inlet and the back wall. This development should allow a sensitivity increase in MEMS mass spectrometers using pumps of moderate capacity.

Keywords: vacuum interface, skimmer, schlieren imaging, micro-jet, bulk micromachining

(Some figures may appear in colour only in the online journal)

1. Introduction

Chemical analysis by mass spectrometry requires ionization of the sample, a process often accomplished at atmospheric pressure. The problem of transferring the ions produced to high vacuum, where they may be mass-analysed using electric and/or magnetic fields, has been an area of relentless investigation [1–4]. In modern instruments, this is achieved using a number of differentially-pumped stages. Ambient gas and ions from the ion source are drawn into the first stage via an orifice or capillary tube. The purpose of the vacuum interface is to transmit ions entrained in the initial gas expansion to the second and subsequent stages efficiently. The introduction by Fenn [5, 6] of skimmer-based interfaces is recognised as a crucial milestone, as it led to the commercial development of electrospray ionisation (ESI) and inductively-coupled plasma (ICP) instruments, two workhorses of modern analytical mass spectrometry.

A number of key mass spectrometer components have been successfully miniaturised using microelectromechanical systems (MEMS) technology. Ion sources, pumps, pressure gauges, detectors, and mass analysers have been reviewed elsewhere [7]. Vacuum interfaces are three-dimensional structures that involve complex gas flow dynamics and overlapping electric fields. Consequently, the development of a vacuum interface using planar processing is a significant challenge, and

there has been little progress to date. A specific difficulty is that gas flow in MEMS is challenging to investigate experimentally. Most efforts have been directed towards flow rate measurements, which are used to validate theoretical modelling [8]. Imaging studies, an important tool in the understanding of gas dynamic problems, are notably absent.

Here, we describe advances in MEMS skimmer-based interfaces, part of a wider effort to develop MEMS mass spectrometry components and complete, miniaturised systems [9–14]. An initial fabrication process and associated characterisation were previously described [15]. However, this work revealed that the interface did not behave in the desired manner. The design has now been modified, resulting in a 70-fold increase in the signal level. A key enabler was the development of a schlieren microscope to image the gas flow within the interface. Exceptionally detailed images have now been obtained, and the nature of the gas flow field has now become clear.

In section 2, supersonic jet formation and shock-free flow sampling using skimmers are reviewed. The design and fabrication of the MEMS skimmer assembly is presented in section 3, together with descriptions of the schlieren imaging and mass spectrometry test systems. Experimental results are presented in section 4, and conclusions are drawn in section 5.

2. Gas dynamics in vacuum interfaces

Detailed descriptions of gas expansion dynamics and interaction of the resulting flow field with a downstream skimmer can be found in standard texts and reviews [2, 3, 16–21]. A brief overview is given here.

Supersonic jets are formed when gas from a high-pressure source passes through an orifice and expands into a low-pressure region. The originally stagnant gas accelerates as the streamlines converge towards the orifice. If the pressure ratio exceeds the choked flow condition, the velocity reaches a value of $M = 1$, where M is the Mach number, at the orifice plane. Downstream of the orifice, the gas expands as a free jet. Collisions during the initial expansion allow thermal energy stored in molecular degrees of freedom to be traded for directed acceleration. The flux angular distribution is consequently strongly peaked in the forward direction, resulting in a much higher centreline intensity than can be obtained from an effusive source. A terminal velocity is attained within a few orifice diameters [2], and the streamlines then become straight, appearing to radiate from a virtual source just in front of the orifice [19].

In supersonic gas dynamics, flow cannot adjust gradually to changing conditions downstream. Disturbances are signalled by sound waves ($M = 1$), which cannot propagate upstream into gas flowing at supersonic velocities ($M > 1$). Instead, flow properties, including direction, density, pressure, temperature and entropy, change abruptly at shocks, which may be oriented obliquely or normal to the upstream flow. Supersonic expansions and shocks have been observed over a staggering range of length scales, spanning supernovae, nuclear weapon detonations, rocket engine exhaust plumes, and (as here) sub-millimeter jets in a MEMS device.

The inertia of the jet pushes back the low pressure gas but the flow must eventually adjust to the ambient conditions at its boundary. This is achieved by a cylindrically symmetric barrel shock terminated in the axial direction by an almost flat normal shock known as the Mach disc. A schematic representation of the shock structure, often referred to as a shock bottle, is shown in figure 1(a). An expansion fan forms around the circumference of the orifice as the gas expands into the low pressure region. Expansion waves propagate outward to the jet boundary where they are reflected as weak compression waves. These coalesce to form the barrel shock [19, 22].

In the axial direction, the Mach number steadily increases while the density, pressure, and temperature decrease. To adjust to the background gas conditions at the Mach disc, the flow must be abruptly slowed so that the energy is redistributed amongst the molecular degrees of freedom. Conservation of mass, energy, and momentum dictate the relation between jet Mach number and the pressure ratio across the shock. As the background pressure is reduced, the jet may expand further and to higher Mach numbers before the Mach disc forms.

The region bounded by the barrel shock and the Mach disc is shielded from interaction with the background gas and is referred to as the zone of silence. The flow passing between the barrel shock and the jet boundary is supersonic, but the Mach numbers are lower than in the jet core. Its direction changes via an oblique reflected shock, anchored to both the barrel shock and the Mach disc at the triple point. Downstream of the triple point, the boundary between the subsonic flow that has passed through the Mach disc and the outer annulus of supersonic flow is marked by a slip line.

Sampling of supersonic flow using a conical skimmer was first proposed by Kantrowitz and Grey [24]. A successful demonstration by Becker and Bier followed shortly thereafter [25]. The motivation was the need for intense molecular beams to investigate chemical reaction dynamics. However, progress was initially hampered by skimmer interference effects. Separated bow shocks in front the skimmer entrance, shock formation within its throat, and scattering from its internal walls all diminished the transmitted beam intensity [26, 27]. Fenn realised that skimmer interference could be eliminated at working pressures below 10^{-3} mbar [23]. In this pressure regime, shock structures disappear and molecular flow conditions prevail at the skimmer, leading to a reduction in scattering losses. In a landmark paper [5], Fenn also demonstrated that molecular beam techniques could be used to couple atmospheric pressure ion sources to mass analysers in vacuum. Compared with existing systems that suffered from low sensitivity due to scattering losses, extracting ions from the initial expansion as a supersonic beam substantially enhanced the efficiency of transfer to downstream ion optics.
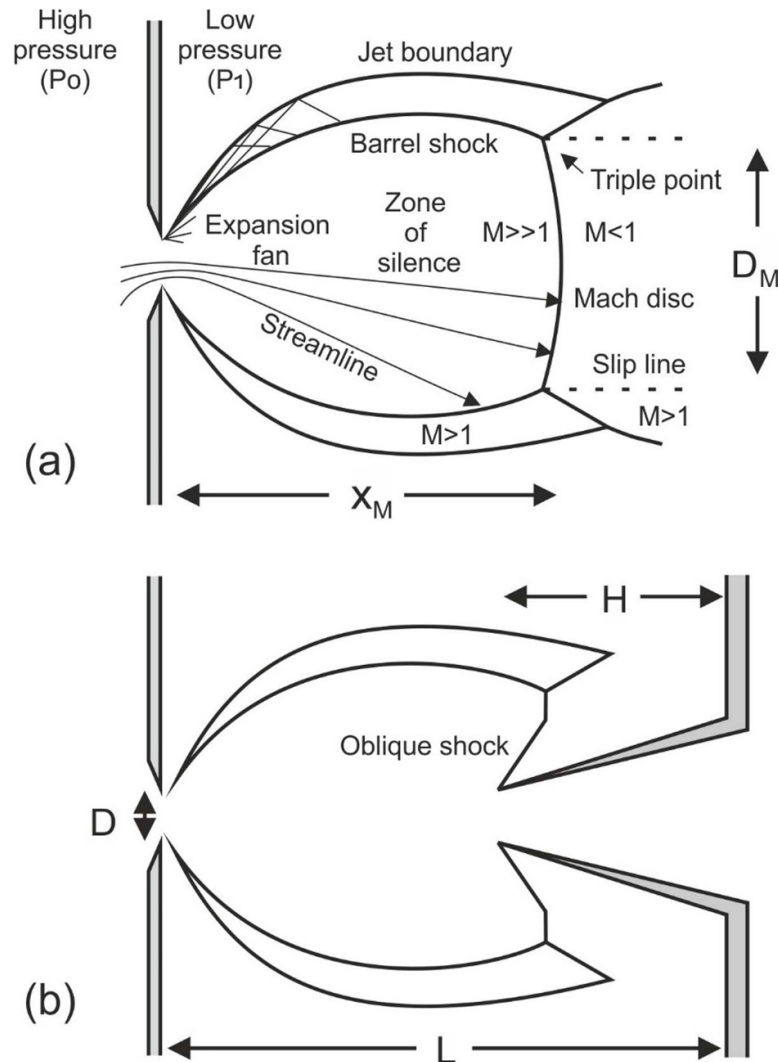
Figure 1. (a) Shock structure of a supersonic free jet expansion. Adapted from [19]. © IOP Publishing Ltd All rights reserved. (b) Sampling of the supersonic flow using a skimmer. Adapted with permission from [23]. Copyright (1984) American Chemical Society.

The use of bulky high vacuum pumps to evacuate the inlet flow at low pressure is unappealing for mass spectrometry. More convenient mechanical pumps necessitate operation in the 1 mbar regime, and consequently, a solution to the challenging aerodynamic problem of extracting a beam from a continuum jet with a fully developed shock structure. If a blunt object is placed in a supersonic flow field, a separated bow shock develops. This must be avoided because the gas re-heats in the shock and collimation is lost. Ideally, peripheral flow should be diverted either side of the skimmer, with the change in direction being accommodated by an oblique shock anchored to the rim, as shown in figure 1(b), leaving the central flow to pass through the skimmer without encountering a normal shock. By systematically investigating sharp skimmers with 2 μm thick rims, Campargue [23] determined that the optimum cone angles for shock-free sampling are 55° (external) and 45° (internal). Mass spectrometer manufacturers have mostly adopted geometries close to these values, though rims appear to be thicker than 2 μm [28].

3. Experimental details

3.1. MEMS interface design and fabrication

The interface is a monolithic, stacked assembly comprising inlet and skimmer dies separated by spacers. An exploded view is shown in figure 2(a). Gas passes through a 100 μm diameter cylindrical inlet channel in the upper silicon die and expands into the first vacuum stage. The jet is intercepted by a thin-walled, open-ended, pyramidal nickel skimmer, and a portion of the flow is transferred to the second vacuum stage. Two skimmer geometries have been fabricated. The method described previously [15] yields 200 μm tall skimmers with 50 × 50 μm entrance apertures. Transfer of the process to thicker wafers has now allowed fabrication of 750 μm tall skimmers with 100 × 100 μm entrance apertures, as shown in figure 2(b). Here, the Ni skimmer cone can be seen surrounded by other vertically etched features.

Figure 3 shows the fabrication process for the skimmer die. The starting point is a 1 mm thick (100) Si wafer, whose
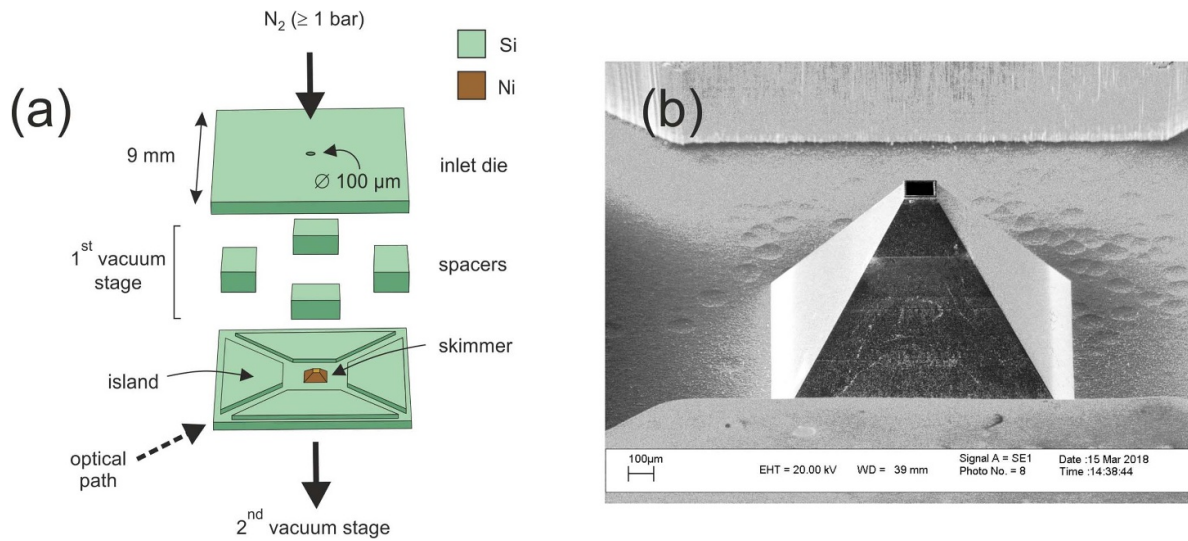
Figure 2. (a) Exploded view of the MEMS vacuum interface showing the stacked assembly of silicon dies. Adapted from [15]. © IOP Publishing Ltd All rights reserved. (b) SEM image of a 750 μm tall Ni skimmer with a 100×100 μm entrance aperture.
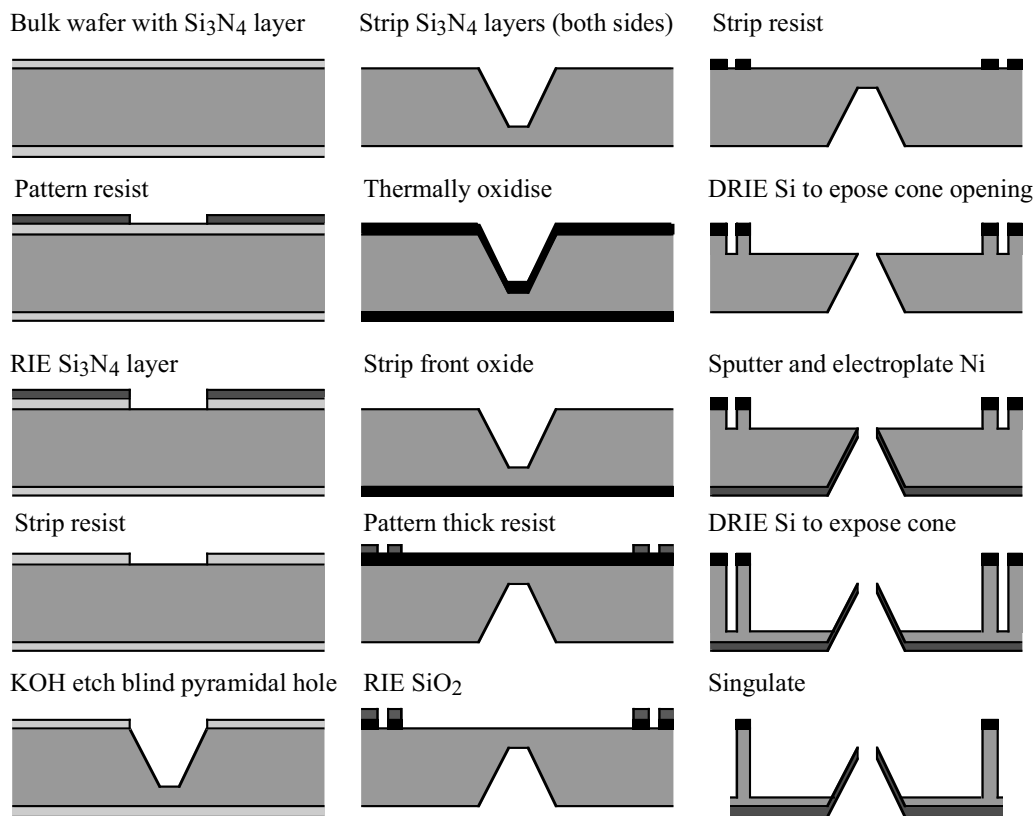

Figure 3. Skimmer fabrication process, based on a combination of anisotropic wet chemical etching and deep reactive ion etching of (100) silicon and electroplating of nickel.

front side is etched to form blind pyramidal holes by anisotropic wet chemical etching in KOH, using Si_3N_4 as a surface mask (LH column). A SiO_2 surface mask is formed on the rear of the wafer to define other features including channels for pumping and schlieren imaging (central column). Deep reactive ion etching (DRIE) from the rear using a Surface Technology Systems single chamber inductively coupled plasma etcher is used to expose the base of the pyramidal hole, RF sputtering and electroplating are used to coat the hole with a thick layer of Ni metal, and further DRIE is used to expose the skimmer cone thus formed and complete the fabrication of additional features (RH column). The inlet die is considerably simpler and formed by patterning and DRIE of Si to form an inlet channel and an outline. Both inlet and skimmer dies
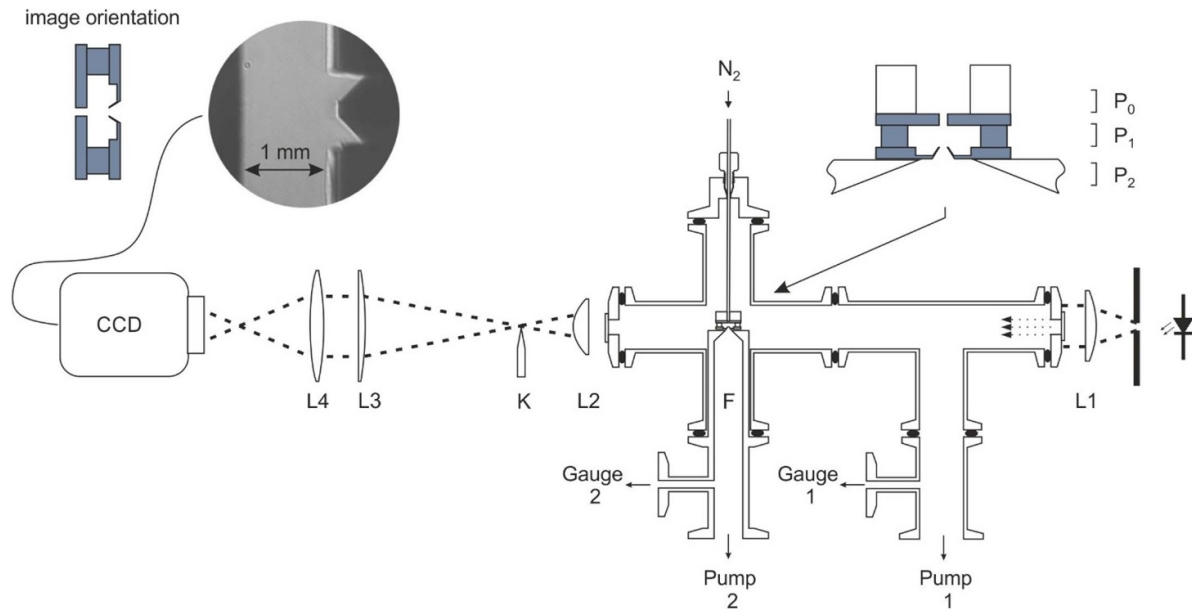
Figure 4. Schlieren microscope for imaging jet interactions with a skimmer in vacuum. Light from a pin hole source is collimated by lens $L1$ and passes through the MEMS skimmer assembly, which is mounted on a differentially pumped finger, F. Lenses $L2$ and $L3$ expand the beam and $L4$ forms an image on the CCD detector. A schlieren image of the gas flow is obtained by moving the knife edge K into the beam at the common focus of $L2$ and $L3$. Adapted from [15]. © IOP Publishing Ltd All rights reserved.

are sputter coated with gold to prevent charge accumulation on the silicon surfaces during mass spectrometry. During final assembly, the inlet channel and skimmer orifice are aligned to within ± 10 μm under a microscope and permanently bonded by applying adhesive across the three layers. However, a more advanced design would incorporate self-alignment features such as ball and socket kinematic mounts [11]. Skimmer assemblies used for mass spectrometry also include polymer tabs under each of the spacer blocks to allow electrical biasing.

3.2. Schlieren imaging

Previously [15], we described a schlieren microscope and presented initial images of supersonic expansions in a MEMS vacuum interface, the first successful imaging of this type. Optimisation of the optical system has now yielded improved resolution.

Figure 4 shows a layout of the schlieren imaging optics and the vacuum system required to operate the MEMS skimmer assembly. The vacuum system is constructed from a vacuum tee and a four-way cross with KF25 flanges. Either a rotary pump (Leybold Trivac D4B) or a scroll pump (Varian SH-110) was used to pump the first stage. The first stage pressure, P_1, was varied using an in-line throttle valve. The skimmer assembly was mounted on a re-entrant vacuum finger (F) pumped by a turbomolecular pump (Pfeiffer HiPace80). Nitrogen was supplied through a stainless steel tube attached to the silicon die using a brass collar and epoxy adhesive. Externally, a connection was made to a gas manifold that could be pressurized to a set pressure using a precision regulator, or pumped out to allow acquisition of a background (jet-off) image.

Some of the work described below relates to jets impinging on flat surfaces in the absence of a skimmer. For these experiments, the vacuum finger F was removed and replaced with a blank end cap. To maintain the same jet orientation, a silicon inlet die was attached to the front face of a plenum chamber mounted on the opposing port. A second gold-coated silicon die was positioned opposite the inlet using four identical pillars to set the spacing at 1.75 mm.

White light from a pinhole source is collimated by lens $L1$. The light enters the vacuum system via a first window, passes through the MEMS skimmer assembly, and exits via a second window. The optical path, which spans 80 cm from source to detector, must be accurately aligned to the narrow but long gap between the two dies of the skimmer assembly. Any misalignment leads to severe narrowing of the field of view. The diameter of the beam exiting the vacuum system is expanded from 4 mm to 20 mm by lenses $L2$ and $L3$. To produce a schlieren image, the beam is partially obstructed by a knife edge at the common focal point of $L2$ and $L3$. Light passing through the gas jet is refracted by the density gradients and is consequently attenuated to a greater or lesser extent by the knife edge. Hence, features of the flow field such as shocks are imaged as light or dark fringes. The best quality images were obtained using a lens $L4$ ($f = 10$ cm) to project a focused image of the skimmer directly on to the CCD detector of the video camera (JVC TK-1280E).

Schlieren images are revealed after frame stacking of the raw video and background subtraction. Light intensity, knife edge position, and camera gain must be adjusted to ensure that no part of the image is at or near saturation. To lessen the effects of drift, 1 min segments of jet-on and jet-off video were recorded alternately until a desired total acquisition

time was reached. Post-acquisition image processing involves subtracting the stacked jet-off video from the stacked jet-on video and then adjusting the contrast and gamma correction to reveal schlieren images. Other investigators have used a ratioing technique [29]. For most images, the signal-to-noise ratio was improved by averaging the RGB layers of the colour video. However, shocks formed at high pressure ratios are very thin and prone to broadening by chromatic aberrations of the optical system. Hence, for these images, a single colour field was extracted. In some cases, the final schlieren image was superimposed on the background to illustrate the position of the jet with respect to the skimmer.

In section 4, schlieren images are correlated with mass spectrometry data. Mass spectra are recorded with the high pressure side at $P_0 = 1$ bar, as the electrospray ion source operates at ambient laboratory conditions. However, for schlieren imaging, P_0 was increased to 3 bar to increase the jet density and decrease the acquisition time. Even at this inlet pressure, the acquisition time for some images exceeded 1 h. Fortunately, geometrical scaling laws for free jet expansions are functions of the pressure ratio, P_0/P_1 [22]. Hence, mass spectra may be correlated with schlieren images recorded at the same P_0/P_1 values, despite the different inlet pressures. However, the jet has less inertia and a lower Reynolds number at $P_0 = 1$ bar. Consequently, viscous effects and differences due to the prevailing flow regime (turbulent or laminar) might not be adequately represented by the schlieren imaging.

3.3. Mass spectrometry

A modified commercial miniature mass spectrometer (MiD4500, Microsaic Systems, Surrey, UK) was used to evaluate the skimmer assemblies. The basic micro-engineered vacuum interface instrument supplied with this instrument, which does not incorporate a skimmer [12, 13], is easily removed. The first stage pumping arrangement was altered to allow access to lower pressures. A new pumping port was drilled close to the inlet and connected to an external rotary pump via a short length of 4 mm i.d. tubing. The effective pumping speed of the tubing was 0.6 l s^{-1} and the base pressure was 3 mbar. To accommodate this modification, the existing source enclosure was removed, and the electrospray module was positioned in front of the inlet using a free-standing clamp. A nitrogen flush was used to prevent ingress of trace volatile contaminants in the laboratory air.

Reserpine was the test analyte for most experiments. Spectra were also recorded for thiabendazole and hexakis(1H, 1H-perfluorobutoxy)phosphazene to confirm ion transmission at low and high *m/z* values, respectively. Reserpine and thiabendazole were both prepared at a concentration of 10 μg ml^{-1} in a 70/30 mixture of acetonitrile and water with 0.1% formic acid; hexakis(1H, 1H-perfluorobutoxy)phosphazene was prepared at 500 μg ml^{-1} in the same solvent. A syringe pump was used to deliver solutions to the electrospray source at a rate of 0.25 μl min^{-1}.

4. Results and discussion

4.1. Free jets and jets impinging on a flat surface

In a conventional vacuum interface, the base of the skimmer, its mounting flange and the back wall of the vacuum chamber are relatively distant from the skimmer entrance. It has long been understood that interference from a stand-off shock generated by these surfaces should be avoided [23, 30]. However, for a MEMS interface, the skimmer should be as short as possible to avoid prolonged etching during fabrication. Our earlier investigation [15] used 525 μm thick wafers, which yielded 200 μm tall skimmers. Schlieren imaging suggested that the Mach disc thickened and merged with the reflected surface shock generated by the back wall of the skimmer die. The skimmer appeared to be engulfed by the shock and there was no evidence of enhanced gas throughput. It was concluded that shock-free skimming would require a taller skimmer.

To interpret the interaction of the flow field with skimmers of different heights, schlieren imaging of millimeter-scale free jets and jets impinging normally on a flat surface has been undertaken. This work provides an insight into the modification of a free jet expansion by a nearby back wall.

Figure 5(a) shows a series of free jet expansions imaged at different P_0/P_1 values. A barrel-shaped shock (bright) and a flat Mach disc (dark) are clearly visible in each image. The Mach disc advances downstream and the barrel shock becomes wider as P_0/P_1 increases. These are the characteristic features of highly under-expanded supersonic jets [22, 31, 32], although slight curvature of the Mach disc is often seen [31, 33, 34].

Images of microjets are scarce. The rainbow schlieren technique has been used to visualise millimetre-scale jets exhausting to atmospheric pressure [34]. Fully developed Mach discs are visible and the jets show a strong resemblance to those in figure 5(a). Moderately underexpanded microjets exhibiting multiple shock cells have been visualised using shadowgraph and schlieren imaging [35–39]. Microjets exhausting into a vacuum environment, again exhibiting multiple shock cells, have also been imaged using laser induced fluorescence [40].

In figure 6, the Mach disc position determined for each of the images in figure 5(a) and three others (not shown) is plotted against P_0/P_1. Ashkenas and Sherman [32] have demonstrated that the position of the Mach disc is related to P_0/P_1 by

$$\frac{x_M}{D} = C\sqrt{\frac{P_0}{P_1}} \qquad (1)$$

where $C = 0.67$ for $15 < P_0/P_1 < 17\,000$. Crist *et al* [22] demonstrated a nearly identical result with $C \approx 0.65$ for $10 < P_0/P_1 < 10^5$. Mach discs as far downstream as $x_M \approx 20$ cm are included in these data sets. It is evident from figure 6 that the position of the Mach disc for millimeter-scale free jets is also in excellent agreement with equation (1). Hence, this investigation, which includes Mach discs at $x_M = 500$ μm,
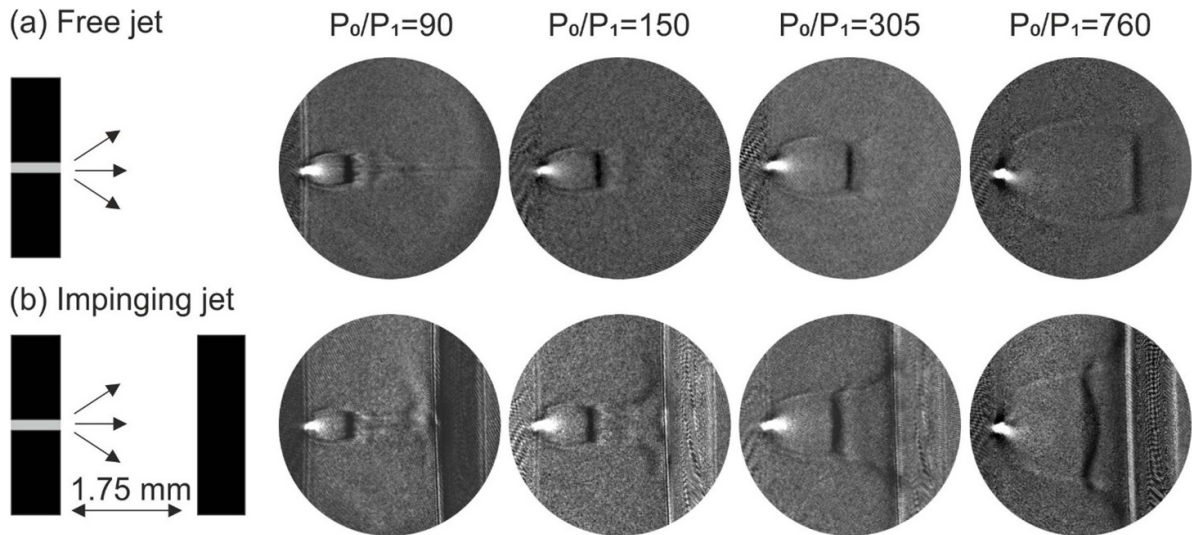
Figure 5. Schlieren images of (a) free jet expansions and (b) jets impinging on a flat surface. The free jet Mach disc evolves into a bowl-shaped surface shock as it moves downstream towards the surface.
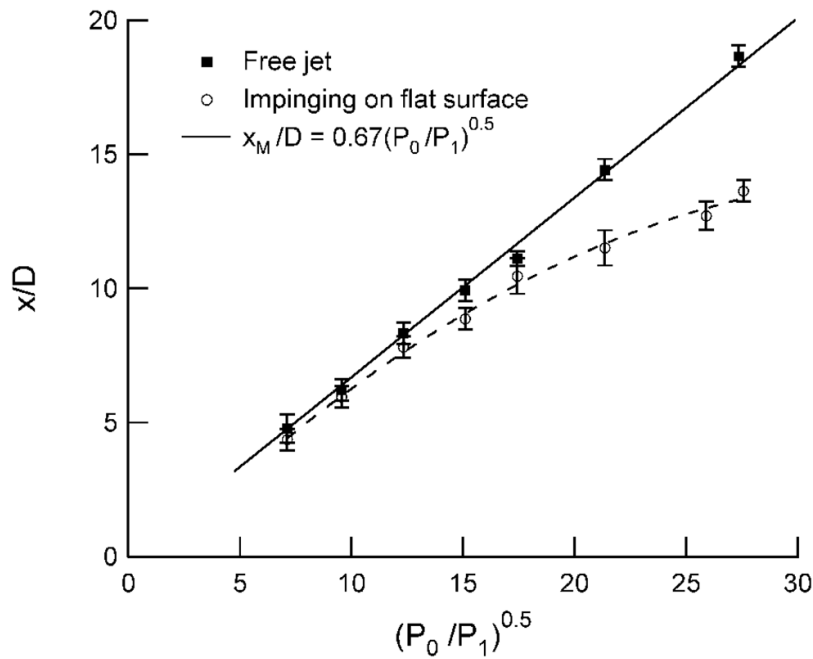

Figure 6. Plots of centreline normal shock position against pressure ratio for a free jet and a jet impinging on a surface located at $x/D = 17.5$. The free jet Mach dis position follows the Ashkenas and Sherman [32] scaling law. The impinging jet surface shock asymptotically approaches a constant stand-off separation.

validates the well-known Ashkenas and Sherman scaling law at much smaller lengths.

The width of the Mach disc, D_M, is a constant fraction of x_M. All four free jets in figure 5(a) may be described by $D_M/x_M = 0.55 \pm 0.02$. This is in excellent agreement with the data of Crist *et al* [22], which shows that, for a convergent nozzle, $D_M/x_M \approx 0.5$ for $100 < P_0/P_1 < 1000$. Similarly, Bier and Schmidt find $D_M/x_M \approx 0.6$ over the same range, again using convergent nozzles [31].

Images of supersonic jets impinging on a flat surface at normal incidence are shown in figure 5(b), for the same pressure ratios. At $P_0/P_1 = 90$ and 150, the shock structure is largely unperturbed by the surface. The flow downstream of the Mach disc eventually impinges on the surface where it is deflected radially. However, at $P_0/P_1 = 305$, the barrel shock is no longer barrel-shaped and the Mach disc appears thickened. The distortion caused by the nearby surface is greater at $P_0/P_1 = 760$, but here the Mach disc has clearly evolved into a bowl-shaped shock. This is imaged as a dark outline and a light infill because the schlieren technique is path-integrating [22, 41]. The interaction of the curved shock with a skimmer will be analysed below. However, it is already clear that previous interpretations [15] of lower quality images in terms of a thick shock engulfing the skimmer will need to

be re-examined. The shock appeared thick because there was insufficient contrast and resolution to discern the curvature of an intrinsically thin shock.

Pairwise comparison of the free and impinging jets reveals that the barrel shocks are foreshortened by a nearby surface but are otherwise nearly identical. The diameter of the impinging jet barrel shock is the same as for the free jet at all points. This is to be expected, given that the supersonic flow generating the barrel shock cannot be affected by a downstream disturbance.

There is a large body of work on the impingement of relatively low-pressure-ratio supersonic jets on surfaces [41–43] arising from interest in aeronautical applications such as vertical take-off [44], and manufacturing processes including coldspray [45] and gas-assisted laser cutting [46]. Highly under-expanded jets impinging on surfaces have received less attention, although investigations have been undertaken relating to rocketry, particularly during early space exploration, when the interaction of retrorockets with the lunar surface was simulated in vacuum chambers prior to the Moon landings. Of particular importance are the schlieren images recorded by Stitt [47] and shadowgraphs by Land and Clark [48, 49]. These images also show distinct bowl-shaped shocks for impinging, highly under-expanded nozzle jets, albeit on a vastly different length scale.

Downstream of the surface shock, the pressure is highest at the centre of the impingement zone as the axial flow velocity must decrease to zero. However, this stagnant, high pressure gas rapidly expands radially, diverting the flow into a wall jet [49, 50]. Consequently, the shape of the surface shock is dictated by conservation of mass, energy, and momentum at the interface between the upstream supersonic expansion and the spatial profile of the downstream flow properties (direction, pressure, density, and temperature). This can be accurately modelled using numerical techniques [49, 50]. The surface shock becomes flattened as it approaches the asymptotic stand-off limit [48, 49]. However, in figure 5(b), the surface shock corresponding to $P_0/P_1 = 760$ has a constant radius of curvature centred on a point within 0–1.5 orifice diameters of the inlet, the expected location of the virtual source from which streamlines radiate [32]. The surface shock must be at all points normal to the supersonic streamlines and, as a result, it can be concluded that the streamlines do not initially change direction on passing through the shock. A schematic representation of the jet, including streamlines passing through the curved surface shock, is shown in figure 7.

Vick and Andrews [51] have examined the evolution of under-expanded impinging jets with pressure ratio, again using schlieren imaging. At lower pressure ratios, a shock similar to a Mach disc was observed, but closer to the nozzle than expected for a free jet. With increasing pressure ratio, the Mach disc evolves into a surface shock whose position asymptotically approaches a fixed stand-off separation. The same behaviour is observed in figure 6, which shows the centreline normal shock position for the impinging jets shown in figure 5(b) and four others (not shown). While the very high pressure ratios used by Vick and Andrews cannot be accessed, it clear that, compared with a free jet, downstream movement of the shock is increasingly impeded by the surface. From
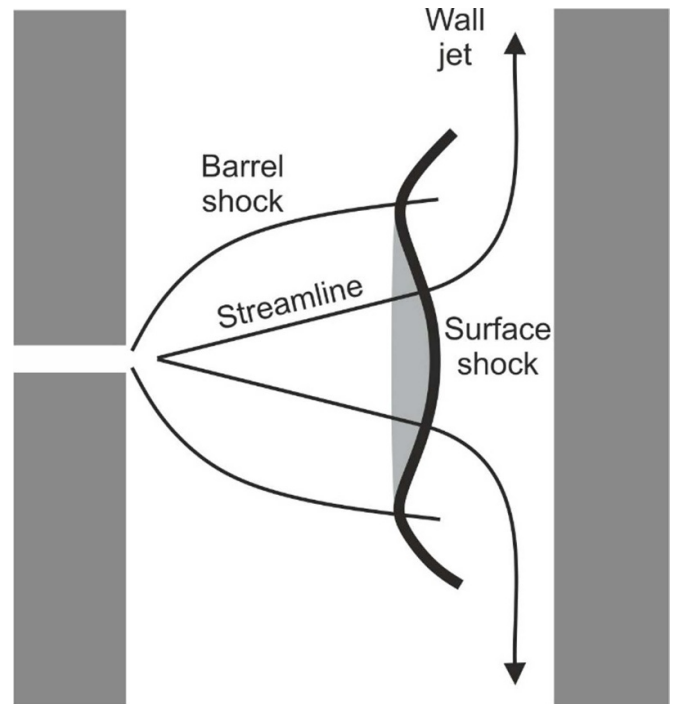

Figure 7. Schematic representation of a supersonic jet impinging on a surface. The flow is diverted into a radial wall jet downstream of the bowl-shaped surface shock.

figure 14 in Vick and Andrews [51] it can be seen that the asymptotic stand-off distance lies in the range 0.08–0.1 L, where L is the distance between nozzle and surface, in agreement with a theoretical treatment placing the shock at 0.08 L [52]. Hence, the position of the surface shock is expected to approach a limiting value of $x/D \approx 16$ in figure 6, a reasonable extrapolation of the plotted data.

These observations are critical to overall system design, particularly the degree of miniaturisation that can be achieved. If the skimmer entrance is relatively close to the back wall, large pumps will be required to pull the shock close enough for attachment. As the asymptotic limit is approached, an order of magnitude increase in pumping capacity yields only a marginal movement of the shock [51]. Clearly, attachment is impossible if the skimmer entrance is within the limiting stand-off separation. In figure 6, the impinging jet shock position begins to deviate from the free jet scaling law by more than an error bar when it is approximately midway across the gap between inlet and surface. Importantly, figure 14 in Vick and Andrews [51] indicates that this is true at other inlet—surface separations, regardless of the absolute value of L. Two design rules can now be stated. Firstly, the skimmer height must be greater than 0.1 L, and secondly, for optimum use of pumping capacity, the skimmer inlet should be no further than 0.5 L downstream of the inlet.

4.2. Shock attachment to microfabricated skimmers

Figure 8 shows schlieren images of supersonic jets interacting with a microengineered skimmer. To allow comparison
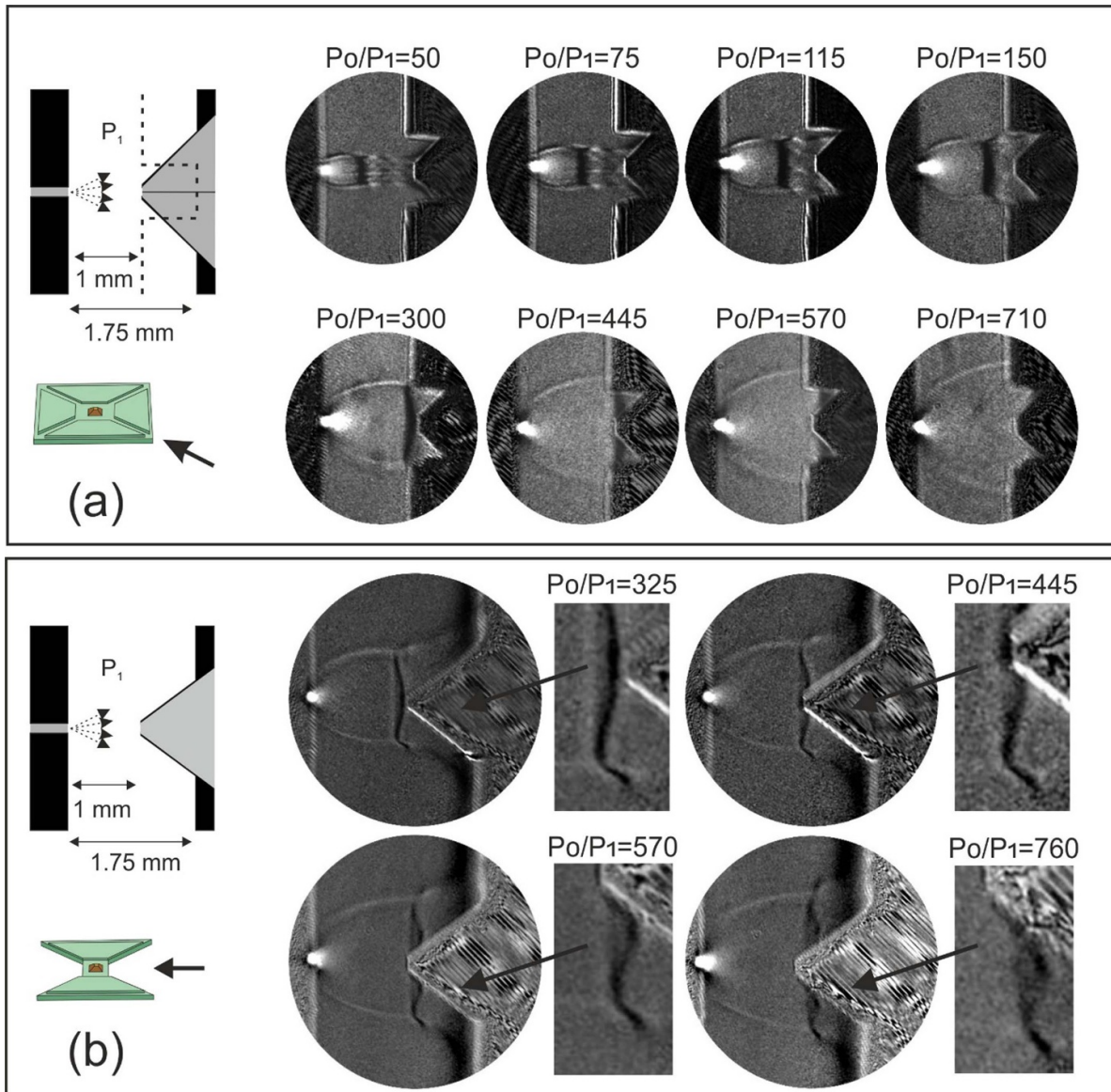
Figure 8. Schlieren images of jet interacting with a 750 μm tall skimmer. In (a) the skimmer is viewed through the channels in the skimmer die. In (b) two of the raised islands have been removed and the viewing angle has been rotated by 45°. At $P_0/P_1 > 445$, the skimmer entrance aperture is within the zone of silence and oblique shocks attach to its rim. There is no evidence of a separated bow shock upstream of the skimmer entrance.

with previous images, the separation between the inlet and the back wall of the skimmer die was set at 1.75 mm, placing the skimmer entrance 1 mm from the inlet. As the field of view is restricted by the channel width, only the top of the skimmer is visible, and the pyramidal skimmer is viewed with a ridge facing the camera. As the pressure ratio increases, the normal shock advances across the gap until it disappears behind raised sections of the skimmer die. At $P_0/P_1 = 50$ and 75, the jet is barrel-shaped and the flow downstream of the Mach disc turns smoothly as it passes either side of the skimmer. For $P_0/P_1 = 115$–300, the back wall begins to influence the jet and the barrel shock is truncated as in figure 5(b). The first four images exhibit bright and dark bands downstream of the Mach disc, suggesting further cycles of expansion and compression. The images corresponding to $P_0/P_1 = 445$–710 show

the normal shock interacting with the skimmer. Although it is impossible to conclude with certainty that an oblique shock is attached to the skimmer entrance, there is no evidence of a detached bow shock.

With the skimmer die securely mounted on the vacuum finger, it was possible to remove two of the raised island sections, leaving the skimmer intact and stabilised by the remaining silicon. This allowed the whole of the skimmer and the back wall to be imaged. A sequence of four images showing the skimmer initially just touching the normal shock and then pushing through into the zone of silence is presented in figure 8(b). Note that a flat face of the pyramidal skimmer is now presented to the camera as the viewing angle has rotated by 45°.

The resolution and contrast of these images allows the flow field to be examined in detail. At $P_0/P_1 = 325$, the curvature of

the normal shock is now more clearly defined. The dark outline represents the thickness of the shock and the lighter infill is a consequence of path-integration. Short oblique shocks anchored to the triple point and extending to the jet boundary can also be seen. As P_0/P_1 is increased, the normal shock deforms into a shape closely resembling the idealised shock attachment shown in figure 1(b) and experimental shadowgraphs of jets impinging on wedges [53]. An oblique shock is attached to the rim of the skimmer entrance but lies close to the skimmer walls. The dark layer close to the back wall in all four images represents the deflected wall jet as in figure 5(b). It becomes darker when the gas passing through the normal shock is joined by gas passing through the annulus beyond the triple point. The images in figure 8 represent a substantial improvement over previous attempts to visualise shock attachment to skimmer cones [23, 54].

The interaction of the rotationally symmetric flow field with the straight edges and corners presented by the pyramidal skimmer is a complex 3D gas dynamic problem. A detailed understanding would require CFD or Monte Carlo simulations. However, the images shown in figure 8 indicate that shock attachment, the fundamental requirement for beam transmission, occurs as it would do for a conventional, circular-section skimmer. No additional shock systems or gas dynamic phenomena are apparent. Other examples of straight-edged skimmers have been reported. Various pyramidal geometries have been successfully employed to generate curtain beams for nuclear physics and molecular spectroscopy applications [55–57], albeit at much lower pressures than used here, and a narrow slit skimmer was used in early molecular beam experiments [24, 58].

The independent pumping applied to the vacuum finger allows the gas flow through the skimmer entrance to be measured and correlated with the schlieren images. An effective pumping speed of $10\ \mathrm{l\ s^{-1}}$ was determined by measuring the pump exhaust flow at representative pressures. Hence, all subsequent P_2 measurements could be converted to absolute gas flow rates (reference temperature = 273.15 K). Figure 9 shows plots of gas throughput for various skimmer assembly configurations, which are labelled A–D. The axis orientation has been chosen so that the interface pressure, P_1, increases from left to right, for easier comparison with the mass spectrometry data presented below.

For configurations A–C (skimmers with $H = 750\ \mu\mathrm{m}$) there is a distinct plateau followed by a sharp upturn in throughput beyond a critical P_0/P_1 value. For D (skimmer with $H = 200\ \mu\mathrm{m}$), P_1 cannot be reduced sufficiently to reveal a plateau, though its onset is recognisable by comparison with the other data sets. The plateau is a known signature of skimmer penetration into the zone of silence. Douglas and French [2] note that increasing the first stage pumping speed of a commercial ICP mass spectrometer by nearly a factor of ten has no effect on the gas flow through the skimmer. This observation is readily understood from figure 1. The flow in the zone of silence is shielded from the background gas by the shock structure, so the centreline flow sampled by

a correctly attached skimmer is independent of P_1. Indeed, P_1 does not appear in any theoretical or empirical equations for centreline flow properties, including density and Mach number [16–18, 32]. When the Mach disc moves upstream of the skimmer entrance at lower P_0/P_1 values, the background gas mixes with the subsonic, post-shock flow, so the density at the skimmer entrance now depends on P_1. Transition to the plateau region occurs when skimmer penetrates the zone of silence. The schlieren images in figure 8 show that for A, this occurs at or close to $P_0/P_1 = 445$, and this is confirmed in figure 9.

The transition to the plateau region shifts to lower P_0/P_1 values as the separation between the inlet and skimmer entrance is reduced from 1000 μm to 500 μm (configurations A–C). This is unsurprising since the location of the Mach disc at the point of attachment must be moved upstream with the skimmer following the trends in figure 6.

The P_1 value required to pull the surface shock on to the skimmer in configuration D is close to an order of magnitude lower than that required for C and only just within the capabilities of the pumping system. A schlieren image corresponding to skimmer penetration into the zone of silence ($P_0/P_1 = 725$) is shown next to the data in figure 9. As expected, transition to the plateau region coincides with skimmer penetration of the surface shock.

4.3. Mass spectrometry

The MEMS vacuum interface has been used to couple an ESI source to a quadrupole mass spectrometer. Both the ESI source and the quadrupoles are fabricated using MEMS techniques and are described in detail elsewhere [10, 11, 13]. In this section, performance characteristics are presented and correlated with the schlieren images and throughput plots.

Electrical biasing of the inlet with respect to the skimmer is essential. During the initial expansion process, solvent from the ESI source forms clusters as the gas temperature decreases. If these are not broken up by accelerating ions to induce energetic collisions, the mass spectrum is dominated by peaks attributable to clusters. In addition, the convergence of field lines at the skimmer entrance results in some focussing of the ions in the zone of silence.

Figure 10 shows how the signal intensity responds to the interface pressure for configurations B, C, and D. The test analyte was reserpine and the signal intensity corresponds to the height of the $[M + H]^+$ peak at m/z 609. The data have been plotted against P_1 rather than P_0/P_1 to give a clearer indication of the pressure regime and pumping capacity needed to operate the interface. The declustering potential was set at 140 V by biasing the inlet and skimmer at +144 V and +4 V, respectively. In the second stage, ions transmitted by the skimmer are focussed by a series of lenses and a quadrupole ion guide. The optimum settings depend on the gas flow through the skimmer and the resulting second stage pressure. Hence, at each P_1 value, the ion optics in the second vacuum stage were optimised to maximise signal. However, collisional focussing
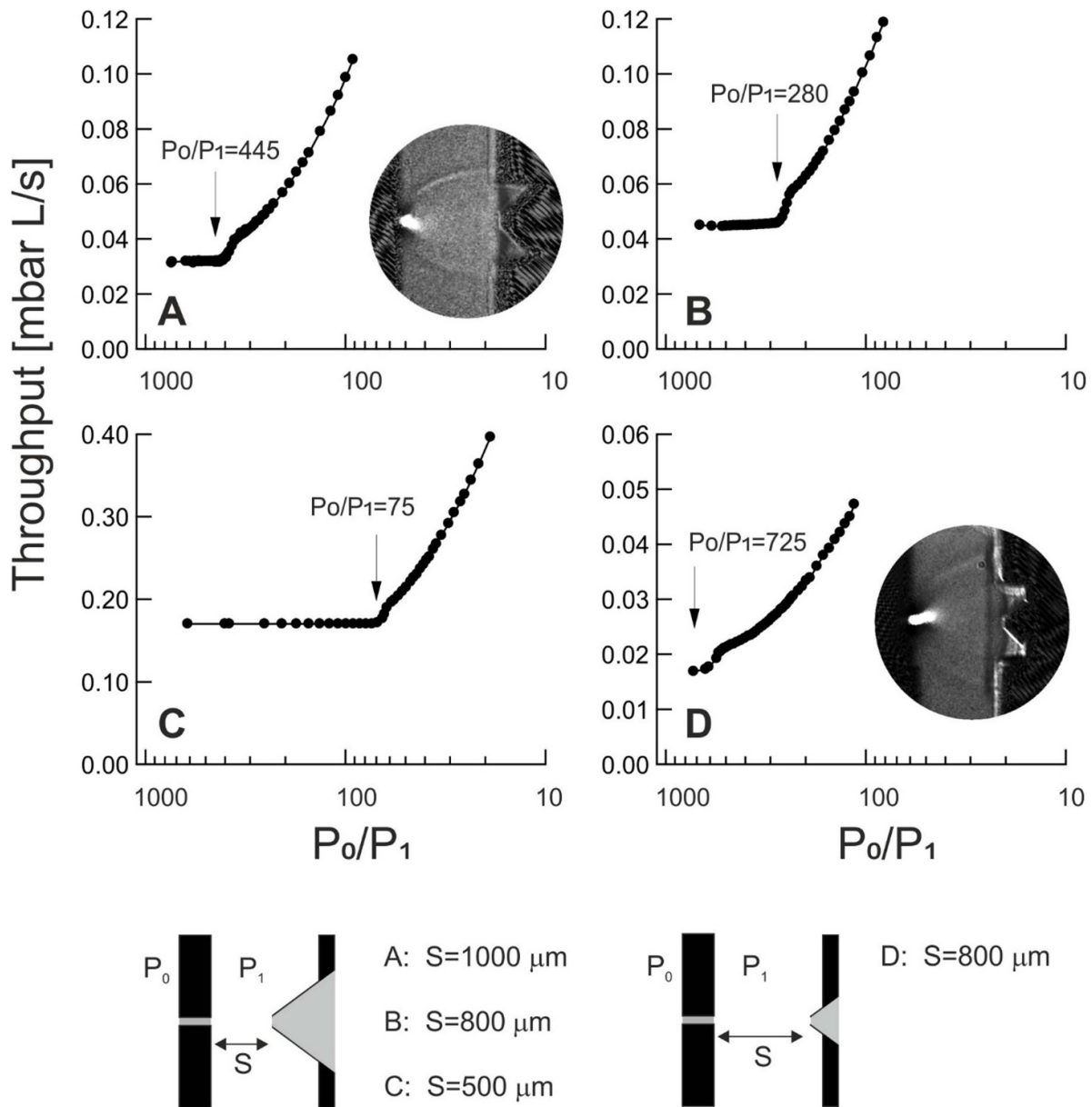
Figure 9. Plots of gas flow through the skimmer against pressure ratio. The skimmer height is 750 μm in configurations A–C and 200 μm in configuration D. The plateau region in each plot is a signature of sampling from the zone of silence. The inset schlieren images for configurations A and D were obtained at $P_0/P_1 = 445$ and $P_0/P_1 = 725$, respectively.

in the ion guide increases with pressure, which may contribute an underlying bias towards operation at higher skimmer gas throughput.

For configuration C, it is clear that the signal is initially approximately level as P_1 is increased from its base value, but sharply decreases at 14–15 mbar. This decrease can be attributed to detachment of skimmer from the shock bottle, since it occurs at the same P_0/P_1 value as transition to the plateau region in figure 9. Although the signal level then rises as P_1 increases, so does the gas throughput. Hence, the signal increases at the expense of second stage gas load. Essentially the same behaviour is observed for configuration B. However,

the characteristic dip and recovery is shifted to lower P_1 values due to the greater separation between inlet and skimmer.

No evidence of skimmer attachment can be seen in data obtained using configuration D. However, figure 9 shows that transition to the plateau occurs at $P_0/P_1 = 725$ as indicated by the arrow in figure 10, well beyond the capability of the mass spectrometer vacuum pump. Hence, the poor performance of 200 μm tall skimmers at base pressure, both here and in previous investigations [15], reflects the inability of the pump to pull the surface shock on to the skimmer entrance. Taller skimmers bring shock attachment into the accessible pressure range, resulting in a 70-fold increase in the signal level.
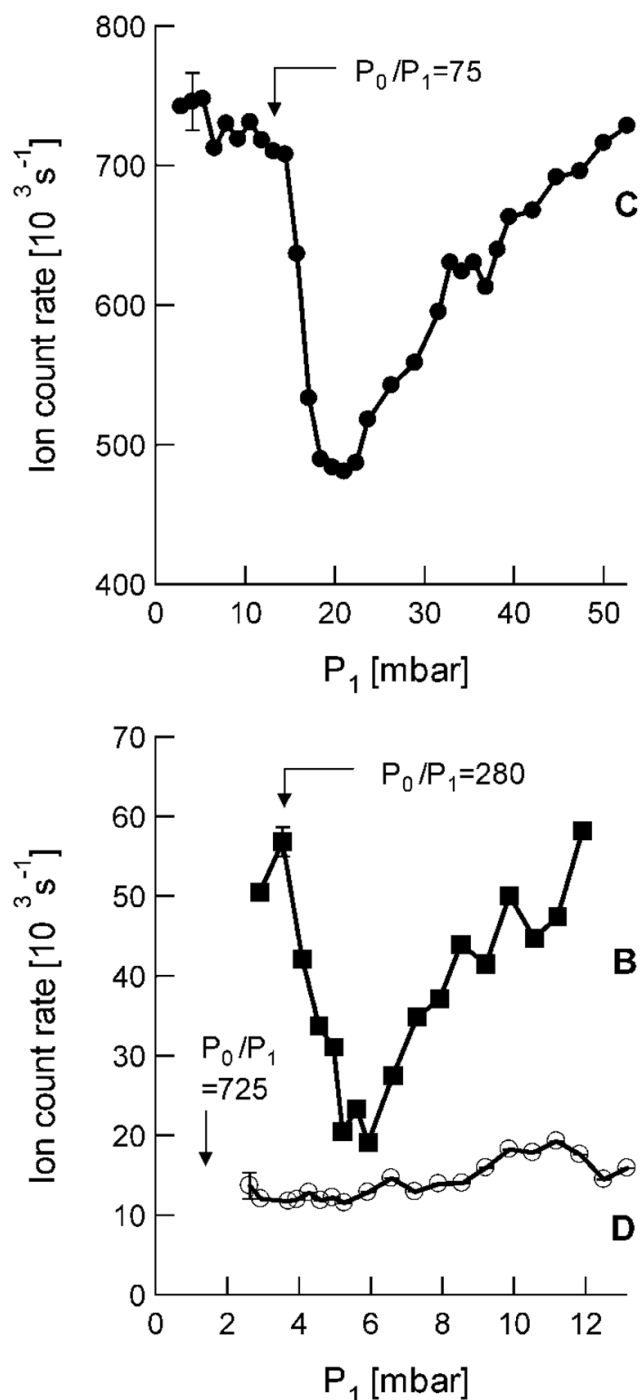
11

Figure 10. Plots of signal intensity at *m/z* 609 against first stage pressure for configurations B, C, and D. The sharp rise in signal at low pressures in the case of B and C corresponds to skimmer attachment and sampling form the zone of silence. The pressure needed to pull the surface shock on to the shorter skimmer is beyond the capabilities of the mass spectrometer pumping system.

In conventional skimmer-based interfaces [2, 28, 59], the working pressure is typically 1–7 mbar and the skimmer entrance is positioned within the zone of silence at 6–12 orifice diameters downstream of the inlet. An important consideration is the local Knudsen number, K_n, at the skimmer entrance

[2, 23]. If $K_n \ll 1$, where $K_n = \lambda/D$ and λ is the mean free path, scattering within the skimmer mouth diminishes the transmitted supersonic flux. Hence, the jet must be sized (by adjusting P_1) and the skimmer positioned such that the jet density is sufficiently low at the skimmer entrance. In configurations A–D, the skimmer aperture is 5–10 orifice diameters downstream of the inlet and penetration into the zone of silence has been demonstrated for pressures as high as 14 mbar. Sampling of high density flow is possible with a microengineered skimmer because the entrance diameter, D, is an order of magnitude smaller than that of conventional skimmers [28]. Moreover, the likelihood of scattering is reduced by the very short throat (10 μm) and wide internal angle (70.6°). A shift of the pressure regime into the range served by compact diaphragm pumps is of considerable importance for system miniaturisation.

Mass spectra of analytes chosen to demonstrate the ability of the interface to transmit ions spanning a wide mass range are presented in figure 11. Configuration C was used with $P_1 = 13$ mbar and $P_2 = 0.0025$ mbar. Similar spectra were also recorded at lower P_1 values. In each case, the inlet bias was set to maximise the signal. As expected for ESI and a correctly functioning interface, each spectrum is dominated by a single peak corresponding to the $[M + H]^+$ ion. The peak width, determined using the full-width at half-maximum (FWHM) definition, is 0.7–0.9. To demonstrate the performance enhancement achieved in this work, a reserpine mass spectrum obtained using a 200 μm tall skimmer in configuration D is also shown, magnified by ×10. The peak width in this case is FWHM = 1.4.

Although the commercial mass spectrometer used during this investigation is a convenient testbed, it is not ideally suited to the gas flow and ion beam characteristics of the skimmer-based interface. For skimmer configuration C, the peak height at *m/z* 609 is 30% of the intensity that can be achieved using the original interface. It is anticipated that a re-design of the second stage ion optics to better exploit the beam collimation would yield significant improvement. Additionally, compared to the standard interface, 85% less gas is passed by the skimmer. Hence, smaller high vacuum pumps are required and further miniaturisation may be realised.

Skimmer-based interfaces are prone to clogging and contamination, leading to a loss of sensitivity over time [60]. The skimmers used here were periodically examined for evidence of material deposition. Even after >100 h exposure to the electrospray plume (with continuous infusion of mostly 10 μg ml^{-1} reserpine), no evidence of bulk material build-up was observed on the internal or external surfaces. Some rainbow discolouration of the skimmer tip was visible, suggesting thin film deposition arising from exposure to accelerated ions and supersonic neutrals. With prolonged use, it is inevitable that involatile analytes and other debris will eventually occlude the inlet capillary and skimmer cone. However, no damage or performance degradation was observed after subjecting the MEMS interfaces to agitation in an ultrasonic bath. Hence, it is anticipated that periodic cleaning will be well-tolerated.
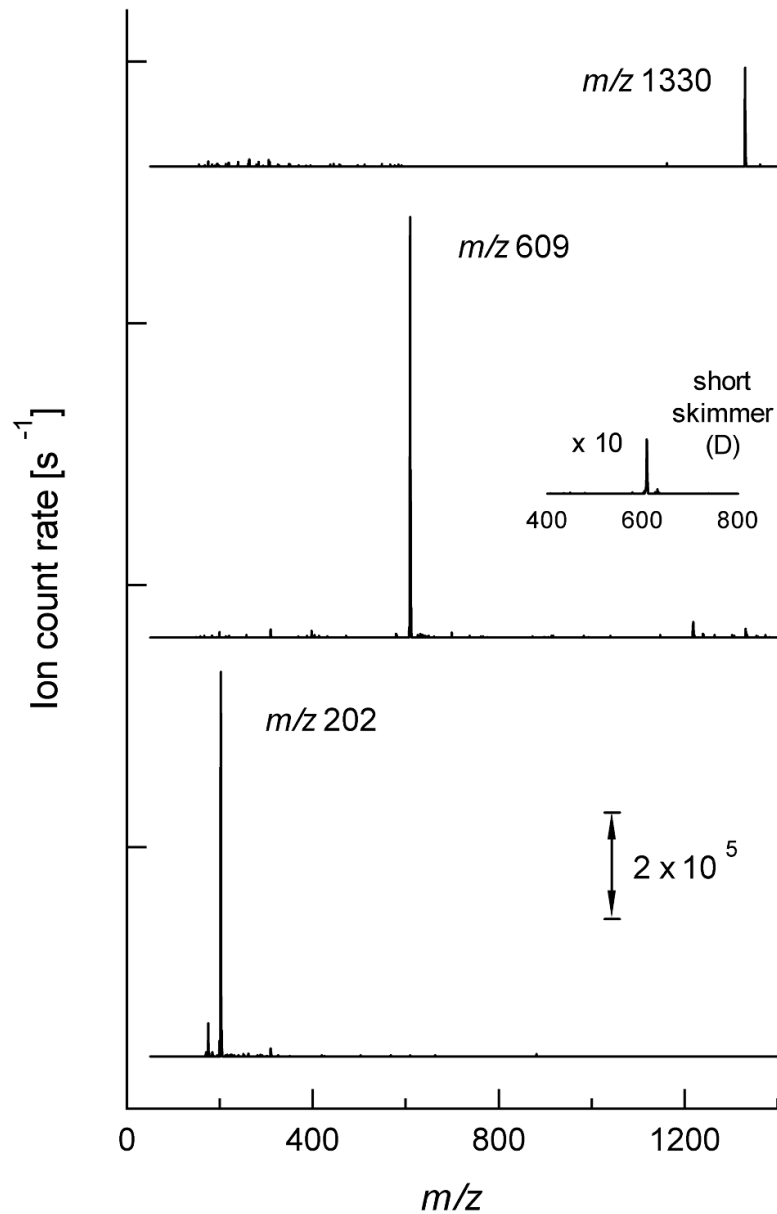
Figure 11. Mass spectra of hexakis(1H, 1H-perfluorobutoxy)phosphazene (top), reserpine (middle), and thiabendazole (bottom) obtained using a 750 μm tall skimmer in configuration C at $P_1 = 13$ mbar. Also shown is a magnified ($\times$10) reserpine mass spectrum obtained with a 250 μm tall skimmer in configuration D at $P_1 = 3$ mbar.

5. Conclusions

Proper skimming of a free-jet expansion within a MEMS vacuum interface has been achieved for the first time. Ion transmission has been demonstrated using a MEMS-based electrospray mass spectrometer. Improved and highly miniaturised schlieren imaging has been used to confirm the critical role of the back wall of the skimmer die. As the operating pressure is reduced, the free jet Mach disc evolves into a bowl-shaped shock that asymptotically approaches a limiting stand-off separation from the back wall, so the location of the skimmer entrance with respect to this shock is a primary design consideration. High pumping speeds in the low mbar regime are required to pull the shock close to the back wall, an unacceptable penalty in a miniaturised system. The relative position of the skimmer entrance within the gap between the inlet die and the back wall of the skimmer die is therefore extremely important. Careful choice of design dimensions has been used to allow shock attachment to a skimmer die fabricated by electroplating inside a pyramidal hole formed by anisotropic etching of 1 mm thick (100) Si wafers, using pumps of moderate capacity. This development should pave the way for future miniaturised mass spectrometers with improved sensitivity. Further improvements may include inlet heating to improve desolvation, and integration of an internal tube lens to focus ions towards the skimmer inlet.

Acknowledgments

ORCID iDs

S Wright ⓘ https://orcid.org/0000-0002-7018-4410
R R A Syms ⓘ https://orcid.org/0000-0003-0901-8314

References

[1] Covey T R, Thomson B A and Schneider B B 2009 Atmospheric pressure ion sources *Mass Spectrom. Rev.* **28** 870–97

[2] Douglas D J and French J B 1988 Gas dynamics of the inductively coupled plasma mass spectrometry interface *J. Anal. At. Spectrom.* **3** 743–7

[3] Farnsworth P B and Spencer R L 2017 Ion sampling and transport in inductively coupled plasma mass spectrometry *Spectrochim. Acta* B **134** 105–22

[4] Bruins A P 1991 Mass spectrometry with ion sources operating at atmospheric pressure *Mass Spectrom. Rev.* **10** 53–77

[5] Yamashita M and Fenn J B 1984 Electrospray ion source. Another variation on the free-jet theme *J. Phys. Chem.* **88** 4451–9

[6] Fenn J B 2000 Mass spectrometric implications of high-pressure ion sources *Int. J. Mass Spectrom.* **200** 459–78

[7] Syms R R A and Wright S 2016 MEMS mass spectrometers: the next wave of miniaturization *J. Micromech. Microeng.* **26** 023001

[8] Perrier P, Hadj-Nacer M, Méolans J G and Graur I 2019 Measurements and modelling of the gas flow in a microchannel: influence of aspect ratios, surface nature, and roughness *Microfluid. Nanofluidics* **23** 97

[9] Geear M, Syms R R A, Wright S and Holmes A S 2005 Monolithic MEMS quadrupole mass spectrometers by deep silicon etching *J. Microelectromech. Syst.* **14** 1156–66

[10] Syms R R A, Zou H, Bardwell M and Schwab M-A 2007 A microengineered alignment bench for a nanospray ionization source *J. Micromech. Microeng.* **17** 1567–74

[11] Wright S, O'Prey S, Syms R R A, Hong G and Holmes A S 2010 Microfabricated quadrupole mass spectrometer with a Brubaker pre-filter *J. Microelectromech. Syst.* **19** 325–37

[12] Wright S, Syms R R A, Moseley R, Hong G, O'Prey S, Boxford W E, Dash N and Edwards P 2010 MEMS-based nanospray-ionization mass spectrometer *J. Microelectromech. Syst.* **19** 1430–43

[13] Malcolm A *et al* 2011 A miniature mass spectrometer for liquid chromatography applications *Rapid Commun. Mass Spectrom.* **25** 3281–8

[14] Wright S *et al* 2015 A microelectromechanical systems-enabled, miniature triple quadrupole mass spectrometer *Anal. Chem.* **87** 3115–22

[15] Wright S and Syms R R A 2018 Supersonic jet interactions with a micro-engineered skimmer *J. Micromech. Microeng.* **28** 085017

[16] Shapiro A H 1953 *The Dynamics and Thermodynamics of Compressible Fluid Flow* vol 2 (New York: Ronald Press)

[17] Liepmann H W and Roshko A 1957 *Elements of Gasdynamics* (New York: Wiley)

[18] Massey B S 1968 *Mechanics of Fluids* (London: Van Nostrand Reinhold)

[19] Jugroot M, Groth C P T, Thomson B A, Baranov V and Collings B A 2004 Numerical investigation of interface region flows in mass spectrometers: neutral gas transport *J. Phys. D: Appl. Phys.* **37** 1289–300

[20] Morse M D 1996 Supersonic beam sources; Chapter 2 *Experimental Methods in the Physical Sciences* vol 29B (Cambridge, MA: Academic Press, Inc) 21–47

[21] Miller D R 1988 Free jet sources; Chapter 2 *Atomic and Molecular Beam Methods* vol 1, ed G Scoles (Oxford: Oxford University Press)

[22] Crist S, Sherman P M and Glass D R 1966 Study of the highly underexpanded sonic jet *AIAA J.* **4** 14–52

[23] Campargue R 1984 Progress in overexpanded supersonic jets and skimmed molecular beams in free-jet zones of silence *J. Phys. Chem.* **88** 4466–74

[24] Kantrowitz A and Grey J 1951 A high intensity source for the molecular beam. Part I. Theoretical *Rev. Sci. Instrum.* **22** 328–32

[25] Becker E W and Bier K 1954 Die Erzeugung eines intensiven, teilweise monochromatisierten Wasserstoff-Molekularstrahles mit einer Laval-Düse *Z. Nat.forsch.* A **9** 975–86

[26] Bird G A 1976 Transition regime behavior of supersonic beam skimmers *Phys. Fluids* **19** 1486–91

[27] Bier K and Hagena O 1966 Influence of shock waves on the generation of high-intensity molecular beams by nozzles *Proc. 3rd Int. Symp. Rarefied Gas Dynamic, Paris (1962) in 'Rarefied Gas Dynamics'* vol 1, ed J A Lauermann pp 478–96

[28] Taylor N and Farnsworth P B 2012 Experimental characterization of the effect of skimmer cone design on shock formation and ion transmission efficiency in the vacuum interface of an inductively coupled plasma mass spectrometer *Spectrochim. Acta* B **69** 2–8

[29] Huang C, Gregory J W and Sullivan J P 2007 A modified schlieren technique for micro flow visualization *Meas. Sci. Technol.* **18** N32–34

[30] Knuth E L 1995 Composition distortion in MBMS sampling *Combust. Flame* **103** 171–80

[31] Bier K and Schmidt B 1961 Zur Form der Verdichtungsstösse in frei expandierenden Gasstrahlen *Z. Angew. Phys.* **13** 493–500

[32] Ashkenas H and Sherman F S 1966 *Rarefied Gas Dynamics: Proc. 4th Int. Symp. Inst. Aerospace Studies, Toronto (1964)* vol II, ed J H DeLeeuw (New York: Academic Press) pp 85–105

[33] Orescanin M M, Prisco D, Austin J M and Kieffer S W 2014 Flow of supersonic jets across flat plates: implications for ground-level flow from volcanic blasts *J. Geophys. Res. Solid Earth* **119** 2976–87

[34] Satti R P, Kohle P S, Olcmen S and Agrawal A K 2007 Miniature rainbow schlieren deflectometry system for quantitative measurements in microjets and flames *Appl. Opt.* **46** 2954–62

[35] Phalnikar K A, Kumar R and Alvi F S 2008 Experiments on free and impinging supersonic microjets *Exp. Fluids* **44** 819–30

[36] Aniskin V M, Mironov S G, Maslov A A and Tsyryulnikov I S 2015 Supersonic axisymmetric microjets: structure and laminar-turbulent transition *Microfluid. Nanofluidics* **19** 621–34

[37] Aniskin V M, Maslov A A, Mironov S G, Tsyryulnikov I S and Timofeev I V 2015 An experimental study of the structure of supersonic flat underexpanded microjets *Tech. Phys. Lett.* **41** 508–10

[38] Scroggs S D and Settles G S 1996 An experimental study of supersonic microjets *Exp. Fluids* **21** 401–9

[39] Hong C, Yoshida Y, Matsushita S, Ueno I and Asako Y 2015 Supersonic micro-jet of straight micro-tube exit *J. Therm. Sci. Tech.* **10** JTST0026

[40] Handa T, Kambara H and Harada M 2017 Visualization of supersonic microjets using LIF and MTV techniques *IOP Conf. Ser.: Mater. Sci. Eng.* **249** 012016

[41] Mitchell D M, Honnery D R and Soria J 2012 The visualization of the acoustic feedback loop in impinging underexpanded supersonic jet flows using ultra-high frame rate schlieren *J. Vis.* **15** 333–41

[42] Lamont P J and Hunt B L 1980 The impingement of underexpanded, axisymmetric jets on perpendicular and inclined flat plates *J. Fluid Mech.* **100** 471–511

[43] Henderson B and Powell A 1993 Experiments concerning tones produced by an axisymmetric choked jet impinging on flat plates *J. Sound Vib.* **168** 307–26

[44] Norum T D 1992 Ground impingement noise of supersonic jets from nozzles with various geometries *J. Aircraft* **29** 993–8

[45] Pattison J, Celotto S, Khan A and O' Neill W 2008 Standoff distance and bow shock phenomena in the cold spray process *Surf. Coat. Technol.* **202** 1443–54

[46] Man H C, Duan J and Yue T M 1998 Dynamic characteristics of gas jets from subsonic and supersonic nozzles for high pressure gas laser cutting *Opt. Laser Technol.* **30** 497–509

[47] Stitt L E 1961 Interaction of highly underexpanded jets with simulated lunar surfaces *NASA Technical Note* D-1095 (Washington, DC: National Aeronautics and Space Administration)

[48] Land N S and Clark L V 1965 Experimental investigation of jet impingement on surfaces of fine particles in a vacuum environment *NASA Technical Note* D-2633 (Washington, DC: National Aeronautics and Space Administration)

[49] Tosh A, Liever P A, Arslanbekov R R and Habchi S D 2011 Numerical analysis of spacecraft rocket plume impingement under lunar environment *J. Spacecr. Rockets* **48** 93–102

[50] Eastman D W and Bonnema J P 1966 Flowfield of a highly underexpanded jet impinging on a surface *AIAA J.* **4** 1302–3

[51] Vick R A and Andrews E H 1966 An investigation of highly underexpanded exhaust plumes impinging upon a perpendicular flat surface *NASA Technical Note* D-3269 (Washington, DC: National Aeronautics and Space Administration)

[52] De La Mora J F, Riesco-Chueca P, Fernandez-Feria R, Fenn J B and Schmitt J J 1986 Collisional energies of heavy species seeded in supersonic H_2 jets impinging on surfaces at large background pressures *Proc. 15th Int. Symp. on Rarefied Gas Dynamics (Grado, Italy)* vol 2, ed V Boffi and C Cercignani (Stuttgart: B. G. Teubner) pp 56–65

[53] Lamont P J and Hunt B L 1976 The impingement of underexpanded axisymmetric jets on wedges *J. Fluid Mech.* **76** 307–36

[54] Gray A L 1989 Visual observation of shock waves in an inductively coupled plasma mass spectrometry expansion stage *J. Anal. At. Spectrom.* **4** 371–3

[55] Hashimoto Y, Fujisawa T, Morimoto T, Fujita Y, Honma T, Muto S, Noda K, Sato Y and Yamada S 2004 Oxygen gas-sheet beam profile monitor for the synchrotron and storage ring *Nucl. Instrum. Meth. Phys. Res.* A **527** 289–300

[56] Subramanian R and Sulkes M 2008 Production of a slit skimmer for use in cold supersonic molecular beams *Rev. Sci. Instrum.* **79** 016101

[57] Tzoganis V, Jeff A and Welsch C P 2014 Gas dynamics considerations in a non-invasive profile monitor for charged particle beams *Vacuum* **109** 417–24

[58] Kistiakowsky G B and Slichter W P 1951 A high intensity source for the molecular beam. Part II. Experimental *Rev. Sci. Instrum.* **22** 333–7

[59] Schneider B B, Douglas D J and Chen D D Y 2001 Ion fragmentation in an electrospray ionization mass spectrometer interface with different gases *Rapid Commun. Mass Spectrom.* **15** 249–57

[60] Douglas D J and Kerr L A 1988 Study of solids deposition on inductively coupled plasma mass spectrometry samplers and skimmers *J. Anal. At. Spectrom.* **3** 749–52